Journal of Materials Chemistry C

Accepted Manuscript

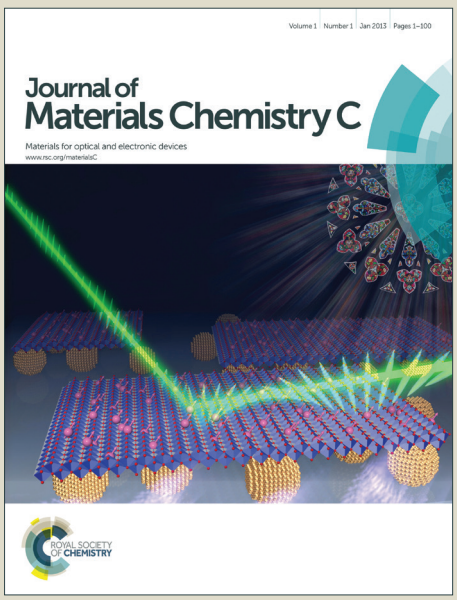

ROYAL SOCIETY OF CHEMISTRY

www.rsc.org/materialsC

Heteroleptic Ir(III) Phosphors with Bis-Tridentate Chelating Architecture for High Efficiency OLEDs

Bihai Tong,[a] Hsiao-Yun Ku,[a] I-Jen Chen,[a] Yun Chi,[a,*] Hao-Che Kao,[b] Chia-Chi Yeh,[b] Chih-Hao Chang,[b,*] Shih-Hung Liu,[c] Gene-Hsiang Lee,[c] and Pi-Tai Chou[c,*]

[a] Department of Chemistry, National Tsing Hua University, Hsinchu 30013, Taiwan; E-mail: ychi@mx.nthu.edu.tw

[b] Department of Photonics Engineering, Yuan Ze University, Chungli 32003, Taiwan; E-mail: chc@saturn.yzu.edu.tw

[c] Department of Chemistry and Instrumentation Center, National Taiwan University, Taipei 10617, Taiwan; E-mail: chop@ntu.edu.tw

---

Abstract

Two tridentate chelates derived from functional 1,3-dipyridin-2-yl benzene, i.e. 1,3-difluoro-4,6-di(pyridin-2-yl) benzene (L1-H), 1,3-difluoro-4,6-di(4-*t*-butylpyridin-2-yl) benzene (L2-H), 1,3-di(pyridin-2-yl)-5-*t*-butylbenzene (L3-H), and 1,3-di(isoquinolinyl)-5-*t*-butylbenzene (L4-H), and 2-pyrazol-3-yl-6-phenylpyridine, i.e. 2-(5-trifluoromethyl-1H-pyrazol-3-yl)-6-(4-trifluoromethylphenyl) pyridine (L5-H_2) and 2-(5-trifluoromethyl-1H-pyrazol-3-yl)-6-(4-*t*-butylphenyl) pyridine (L6-H_2), are synthesized. These chelates are classified as the monoanionic and dianionic chelates according to the number of active hydrogen atoms present. Treatment of L1-H – L4-H with $IrCl_3 \cdot 3H_2O$ afforded chloro bridged dimers $[Ir(Ln)Cl(\mu\text{-}Cl)]_2$ (n = 1 – 4); upon incorporation of secondary chelates L5-H_2 and L6-H_2, it gave formation of six judiciously selected, charge-neutral, bis-tridentate Ir(III) complexes, cf. [Ir(L1)(L5)] (**1**), [Ir(L2)(L5)] (**2**), [Ir(L3)(L5)] (**3**), [Ir(L3)(L6)] (**4**), [Ir(L4)(L5)] (**5**), and [Ir(L4)(L6)] (**6**).

Detailed characterization and photophysical measurement have been performed, and computational calculations were executed to shed light on the enhanced emission efficiency and color tunability. This work further investigated green-emitting and red-emitting organic light-emitting diode (OLED) applications of Ir(III) complexes **1** and **5**, respectively. As a result, a maximum external quantum efficiency of 13.2%, luminance efficiency of 41.4 cd/A, and power efficiency of 35.5 lm/W was obtained for the green OLED (complex **1**), as opposed to 15.4%, 21.0 cd/A, and 16.3 lm/W for the red-emitting OLED device (complex **5**). The high electroluminescence efficiencies suggest great potential of the titled complexes for applications in multicolor OLED displays.

Introduction

Organic light emitting diodes (OLEDs) have been widely investigated for the applications such as full color displays and solid state luminaries, among which, late transition-metal phosphors are known to exhibit higher electroluminescent efficiency versus that of organic fluorescent emitters, because the latter can only utilize up to 25% of the total excitons (i.e. only the singlet excitons). In contrast, the strong spin-orbit coupling imposed by the third-row transition-metal elements would promote an efficient singlet/triplet intersystem crossing, and allow efficient harvest of both singlet and triplet excitons generated during electrical excitation, which, in theory, gives rise to an unitary internal quantum efficiency.[1] In this regard, iridium complexes bearing three bidentate cyclometalates have attracted much attention because of their great potential to exhibit both high luminescent efficiency and adequate color tunability.[2-4] The Ir(III) metal complexes such as $[Ir(piq)_3]$,[5] $[Ir(ppy)_3]$[6, 7] and FIrpic,[8, 9] where piqH, ppyH and FIrpic are 2-phenylisoquinoline, 2-phenylpyridine and bis[2-(4,6-difluorophenyl)pyridinato-C^2,*N*](picolinato)iridium(III), are three representative examples that exhibit red, green and blue emission, respectively.

To date, Ir(III) phosphors bearing three bidentate chelates in both the homoleptic and heteroleptic forms are common.[10-12] Typical synthetic strategies involve the prior preparation of dimers with formula $[Ir(C^N)_2(\mu\text{-}Cl)]_2$ via treatment of heteroaromatics (C^N)H with $IrCl_3{\cdot}3H_2O$. After then, addition of the third identical chelate (C^N)H or distinctive anionic ancillary (L^X)H afforded the anticipated homoleptic and heteroleptic complexes $[Ir(C^N)_3]$ and $[Ir(C^N)_2(L^X)]$, respectively.[3] Parallel to these endeavors, Williams et al. have synthesized the Ir(III) complex [Ir(dpyx)(ppy)Cl],[13] in which dpyx denotes tridentate 1,3-bis(2-pyridyl)-4,6-dimethylbenzene, and reported the possession of higher emission efficiency (Φ = 0.76) versus the *tris*-bidentate analogue *fac*-$[Ir(ppy)_3]$ (Φ = 0.40). Haga et al. have also shown successful preparation of analogous Ir(III) complexes with single tridentate chelate, plus one extra bidentate and monodentate ligand (i.e. 3+2+1 coordination mode).[14-18] Studies on the preparation of Ir(III) complexes with solely the tridentate chelates, i.e. *bis*-tridentate Ir(III) complexes, have been executed but with limited success.[19] In fact, due to difficulty in balancing the 3+ change of Ir(III) center, the Ir(III) complex [Ir(dpyx)(dppy)] and analogues remain as the only class of charge-neutral *bis*-tridentate Ir(III) complex documented in literature. Hence, assessment in OLED fabrications was not attempted to the best of our understanding.

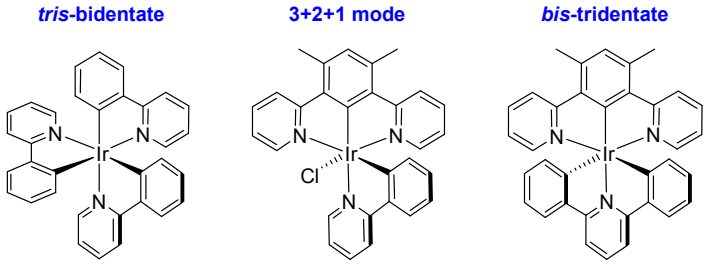

$[Ir(ppy)_3]$ [Ir(dpyx)(ppy)Cl] [Ir(dpyx)(dppy)]

Generally speaking, due to the absence of chelates with lower denticity, this new class of complexes is expected to be more robust than both the *tris*-bidentate and the aforementioned 3+2+1 counterparts, and is thus beneficial to the fabrication of durable OLED phosphors. Therefore, it becomes demanding to develop a suitable

synthetic process for these rarely reported *bis*-tridentate Ir(III) complexes. With this in mind, we proceed to investigate the generalized synthetic and color-tuning protocols, namely: (i) how to achieve good synthetic selectivity and hence better product yield,[20] (ii) how to optimize color tunability and luminous efficiency,[21] and (iii) how to obtain the charge-neutral coordination architectures for better volatility.[22-24]

In the present article, we describe the utilization of monoanionic tridentate pro-chelate, i.e. 1,3-difluoro-4,6-di(pyridin-2-yl) benzene (L1-H), 1,3-difluoro-4,6-di(4-*t*-butylpyridin-2-yl) benzene (L2-H), 1,3-di(pyridin-2-yl)-5-*t*-butylbenzene (L3-H), and 1,3-di(isoquinolinyl)-5-*t*-butylbenzene (L4-H),[25] as well as dianionic tridentate pro-chelate, namely: 2-(5-trifluoromethyl-1H-pyrazol-3-yl)-6-(4-trifluoromethylphenyl) pyridine (L5-H_2) and 2-(5-trifluoromethyl-1H-pyrazol-3-yl)-6-(4-*t*-butylphenyl) pyridine (L6-H_2) in synthesizing these *bis*-tridentate Ir(III) phosphors. The monoanionic chelates (i.e. L1-H – L4-H) are known to react with the Ir(III) source $IrCl_3 \cdot 3H_2O$ in forming the isolable intermediates with formula $[Ir(N^C^N)Cl(\mu\text{-}Cl)]_2$,[26] if the competitive cyclometalation at C4/C6 of central benzene group were adequately blocked.[27] Moreover, the dianionic pro-chelates with single (cf. L5-H_2 and L6-H_2) or even dual pyrazolyl fragments are also reported to be capable of coordinating to the isoelectronic Ru(II) and Os(II) metal atoms, giving a tridentate coordination mode.[28-30] We therefore anticipated that the sequential attachment of these monoanionic and dianionic chelates to the Ir(III) metal center would afford the desired, charge-neutral, *bis*-tridentate complexes with high yield and good color tunability. This approach allows the full exploration of the associated photophysical and OLED performance characteristics, both will be elaborated in the following sections.

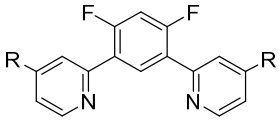

L1-H, R = H; L2-H, R = Bu^t

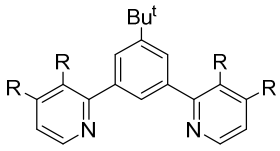

L3-H, R,R = H,H
L4-H, R,R = benzo

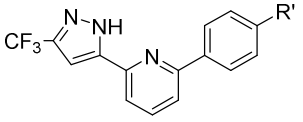

L5-H_2, R' = CF_3; L6-H_2, R' = Bu^t

Results and Discussion

Synthesis and structural characterization. The demanded 1,3-dipyridin-2-yl benzene ligands, namely: L1 – L4, were synthesized using corresponding 1,3-benzene-diboronic ester and 2-bromopyridine derivatives using Suzuki-Miyaura cross-coupling. The required chelates were obtained in high yields, for which the selected syntheses are given in the electronic supporting information. These chelates are known to form the monoanionic tridentate bonding mode upon reacting with the Ir(III) metal source reagent.[31] Therefore, reaction of $IrCl_3 \cdot 3H_2O$ with L1-H – L4-H (1 equiv) in mixed methoxyethanol and water at reflux for 12 h afforded a single product, which, after precipitation, was characterized as $[Ir(Ln)Cl(\mu\text{-}Cl)]_2$, n = 1 – 4, by routine ^1H and ^{19}F NMR analyses.

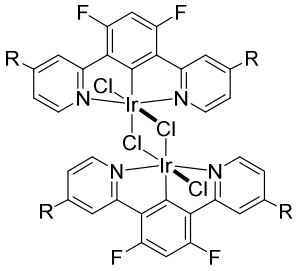

$[Ir(L1)Cl(\mu\text{-}Cl)]_2$, R = H
$[Ir(L2)Cl(\mu\text{-}Cl)]_2$, R = Bu^t

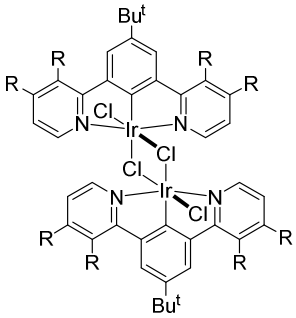

$[Ir(L3)Cl(\mu\text{-}Cl)]_2$, R,R = H,H
$[Ir(L4)Cl(\mu\text{-}Cl)]_2$, R,R = benzo

Moreover, for constructing the charge neutral, *bis*-tridentate Ir(III) complexes, it requires another class of chelates which is subject to the loss of two protons upon reacting with the transition metal element. One obvious design is the 2,6-diphenylpyridine ($(dppyH_2)$, so that a charge-neutral Ir(III) complex

[Ir(dpyx)(dppy)] is formed, for which the dppy is bound to the metal through two carbon and one nitrogen atoms, respectively.[27] In this study, we alternatively switched to the functional 2-pyrazol-3-yl-6-phenylpyridine, L5-H_2 and L6-H_2, due to their greatly increased reactivity for the pyrazole versus phenyl group, such that the synthetic manipulation can be conducted in absence of silver chloride scavenger and at lower temperature.[21] Accordingly, treatment of the aforementioned Ir(III) dimers with either L5-H_2 or L6-H_2 in decalin and in presence of sodium acetate (NaOAc) afforded six *bis*-tridentate Ir(III) metal complexes **1** – **6** in high yields; their structural drawings are depicted below:

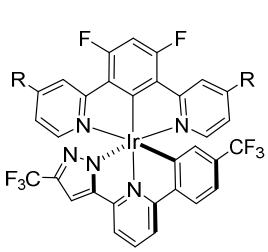

(**1**): [Ir(L1)(L5)], R = H
(**2**): [Ir(L2)(L5)], R = Bu^t

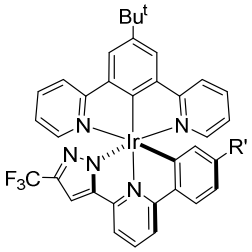

(**3**): [Ir(L3)(L5)], R' = CF_3
(**4**): [Ir(L3)(L6)], R' = Bu^t

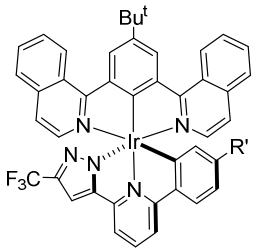

(**5**): [Ir(L4)(L5)], R' = CF_3
(**6**): [Ir(L4)(L6)], R' = Bu^t

Notably, the addition of NaOAc is critical for promoting the reactions with the second chelates.[32-34] Without this basic promoter, the reactions proceeded sluggishly and gave lower product yields. It is believed that coordination through the nitrogen atom of pyrazole, together with central pyridine donor, must be kinetically favorable to the reaction at the *ortho*-carbon of phenyl substituent. The formation of a bidentate N^N coordination mode, similar to that reported for the Ru(II) metal complexes,[35] facilitates the otherwise difficult C-H activation of phenyl substituent in affording the final Ir(III) complexes.

Single crystal X-ray diffraction study of Ir(III) complexes **1** and **5** confirms the *bis*-tridentate mode and the mutually orthogonal orientation of the chelates (Figures 1 and 2). Complex **1** shows the planar arrangement for the monoanionic L1 chelate with non-linear bite angle of C(1)-Ir-N(2) = 156.7(3)° and N(4)-Ir-N(5) = 160.5(3)°, whilst the bond angle between the central coordination atoms of these chelates is

essentially linear, cf. C(17)-Ir-N(1) = 177.1(3)°. Moreover, the Ir-C(17) and Ir-N(1) distances of the dianionic chelate L5 in **1** (e.g. 1.919(9) and 2.063(8) Å) are comparatively shorter than all other Ir-C (Ir-C(1) = 2.035(9) Å) and Ir-N (2.060(6) ~ 2.119(6) Å) distances observed in this molecule as a result of the internal constraint and the *trans*-influence imposed by the opposite donor atom.

In complex **5**, both tridentate ligands show relevant non-linear bite angles (Figure 2), whilst the 1-isoquinolinyl moieties of L4 reveal planar geometry and squeeze the central benzene ring to an out-of-plane configuration by relieving the shortened H···H contacts.[25, 36] As for the second L5 chelate, both the dihedral angles and the bond lengths are similar to those found in previously discussed **1**, with an elongated Ir-N(2) pyrazolyl distance (2.113(6) Å) due to the *trans*-influence of the cyclometalated phenyl fragment.

Photophysical data. The UV-Vis absorption and emission spectra at RT were recorded (Table 1). A comparison of absorption features among these Ir(III) complexes is shown in Figure 3, in which all titled complexes exhibit very strong absorption bands below 320 nm ($\varepsilon > 2 \times 10^4$ $M^{-1}\cdot cm^{-1}$) due to $^1\pi\pi^*$ transitions localized on both the tridentate chelates, together with a set of intense bands in the region < 380 nm ($\varepsilon > 8 \times 10^3$ $M^{-1}\cdot cm^{-1}$), which are attributed to MLCT transitions from central Ir(III) ions to either tridentate chelates. Compared with Ir(III) complexes **1** and **2**, replacing the electron-withdrawing fluoro substituents in L1 with the electron donating *t*-butyl substituent in L3, giving complexes **3** and **4**, leads to a substantial red-shifting in ^{1}MLCT transition energy from ~395 nm to ~430 nm, the result of which also confirms the dominance of L3 chelate in forming the lower energy absorption. Further substitution of pyridyl groups in L3 with 1-isoquinolinyl moieties, forming the L4 chelate as observed in both **5** and **6**, gives the most red-shifted ^{1}MLCT absorptions among all complexes with peak wavelength located at ~490 nm. In all cases, the lowest energy peaks ($\varepsilon \sim 1 \times 10^3$ $M^{-1}\cdot cm^{-1}$), or the lower energy shoulders of the ^{1}MLCT transition, can be assigned to the spin-forbidden

^{3}MLCT absorptions with partial contribution derived from the $^3\pi\pi^*$ transitions.

Figure 3 depicts the emission spectra of the titled complexes, which are also strongly affected by the variation of chelates. As can be seen, Ir(III) complexes **1** and **2** showed the most blue-shifted emission. Moreover, introduction of the electron-donating t-butyl substituent to the terminal pyridyl fragments of L1 in complex **1**, forming L2 and hence the corresponding Ir(III) complex **2**, slightly red shifts the emission peak wavelength from 490 to 493 nm. Their structured emission profiles suggest the notable contribution of ligand-centered $\pi\pi^*$ transitions in both **1** and **2**. On the other hand, replacing the electron-withdrawing fluoro substituents in the central benzene ring of L1 with the electron donating *t*-butyl substituent in L3 lowers the emission energies to 505 and 515 nm for **3** and **4**, respectively. The result can be rationalized in terms of the increase of electron density at the central benzene fragment and hence decrease of the ligand-centered $\pi\pi^*$ electronic transition. Similarly, introduction of 1-isoquinolinyl moieties concurred with the most red-shifted emission observed for Ir(III) metal complexes **5** and **6**. Such an effect in extending the π-conjugation has been observed for many luminescent Os(II), Ir(III) and Pt(II) metal complexes.[37-41]

In order to gain more fundamental insight into the above experimentally observed absorption and emission spectra, we then performed the time-dependent density functional theory (TD-DFT) calculations. For the Ir(III) complexes **1 – 6**, the frontier molecular orbitals mainly involved in the lowest singlet and triplet optical transitions are displayed in Table 2 and Figure 4 (HOMO, LUMO and LUMO+1). Also, the calculated wavelengths and the charge characters of the five lower lying singlet and triplet optical transitions as well as the corresponding molecular orbitals are listed in Table 2, S1 – S6 and Figures S1 – S6 of supporting information, respectively. The calculated wavelengths of the $S_0 \rightarrow S_1$ transitions for **1**: 389.8 nm, **2**: 392.3 nm, **3**: 415.9 nm, **4**: 421.8 nm, **5**: 473.8 nm, and **6**: 482.5 nm (in CH_2Cl_2) are close to the observed onsets of each absorption spectrum measured in CH_2Cl_2 (cf. Figure 3 and

Table 2). Moreover, the calculated wavelengths of the $S_0 \rightarrow T_1$ transitions for **1**: 454.6 nm, **2**: 456.1 nm, **3**: 483.7 nm, **4**: 490.8 nm, **5**: 567.3 nm, and **6**: 574.8 nm also correlate well to the onset of the phosphorescence shown in Figure 3. Therefore, both computational level and functional used for TD-DFT calculations in this study prove to be adequate for the titled Ir(III) *bis*-tridentate complexes.

According to the analyses (Table 2), the $S_0 \rightarrow S_1$ and $S_0 \rightarrow T_1$ optical transitions for the Ir(III) complexes **1** – **6** are majorly assigned to the HOMO → LUMO or HOMO → LUMO+1 and their metal-to-ligand charge transfer (MLCT) contribution is significant, which is within 20.16% (T_1 state of **1**) to 31.38% (T_1 of **4**). On the one hand, the electron density distributions of HOMO for the Ir(III) complexes **1** and **2** are mainly located at the pyrazolate and phenyl moieties of the 2-pyrazol-3-yl-6-phenylpyridine chelate, the Ir(III) metal center and in part the central benzene moiety of the 1,3-di(pyridin-2-yl) benzene chelate. On the other hand, the electron density distributions of LUMO (and LUMO+1) are mainly located at the entire 1,3-di(pyridin-2-yl) benzene chelate. In other words, the lowest lying transition in both singlet and triplet manifold is rather complicated for complexes **1** – **6**, incorporating all metal-to-ligand, intra-ligand and ligand-to-ligand charge transfer contributions, denoted as MLCT, ILCT and LLCT, respectively. Similar type of transition character is also resolved for complexes **3** and **4** (see Table 2 and Figure 4) except that the central benzene moiety of the 1,3-di(pyridin-2-yl) benzene chelate contributes more to HOMO due to its lifted π-energy level via electron donation property of the *t*-butyl substituent. This leads to the lowering of $S_0 \rightarrow S_1$ transition (cf. **1** and **2**, see Table 2), consistent with the experimental observation (see Figure 3). Upon replacing two pyridinyl fragments in the 1,3-di(pyridin-2-yl) benzene chelate by two isoquinolines, yielding complexes **5** and **6**, the calculation results indicate a much less contribution to HOMO by pyrazolate and phenyl moieties of the 2-pyrazol-3-yl-6-phenylpyridine chelate (cf. complexes **1** and **2**, see Figure 4). On the other hand, LUMO of **5** and **6** is largely located at the isoquinolinyl sites. From the

chemistry point of view, this result can be rationalized by the elongation of π-conjugation in the isoquinolinyl moiety, leading to the increase (decrease) of the π-bonding orbital (π* antibonding orbital) energy. The net result is to decrease the ππ* and MLCT energy gap and consequently the significant red shift of the absorption/emission for **5** and **6** compared with complexes **1** – **4**.

The radiative (k_r) and nonradiative decay (k_{nr}) rates are deduced from the Φ and τ data using the equations:

$(k_r + k_{nr}) = 1 / \tau_{obs}$ and $\Phi\ (\%) = k_r / (k_r + k_{nr})$

for which the calculated data are also listed in Table 1. Complexes **1** and **2** are strongly luminescent with quantum yield Φ = 0.72 and 0.64 and luminescence lifetime τ = 1.81 and 3.37 μs at RT, respectively. Lowering of solution emission efficiency was observed for **3** and **4**, which can be attributed, in part, to the intrinsic vibrational and rotational motion of *t*-butyl group on central benzene unit of L3, which introduced faster radiationless deactivation, as indicated by their nonradiative decay rate constant k_{nr} of 4.90×10^5 and 9.63×10^5 s^{-1} for **3** and **4**, respectively, which are the largest two k_{nr} values among the titled complexes (Table 1). For the 1-isoquinolinyl substituted Ir(III) complexes **5** and **6**, the extended π-system of L4 further improved to the emission efficiency to 0.63 and 0.43, respectively, which are perhaps due to the greater aromatic π-conjugation and hence the reduced variation of C-C distances in the excited states versus the ground state. The k_r values of all Ir(III) complexes range between 1.90 and 3.56×10^5 s^{-1}, whilst the k_{nr} values span the range (1.07 to 9.63×10^5 s^{-1}), both are strongly structure-dependent. Moreover, since both Ir(III) complexes **1** and **5** showed the highest emission efficiencies, they were selected as dopant emitters for fabrication of OLED devices.

Electrochemistry. The electrochemical behavior of these Ir(III) complexes was measured, for which the numerical redox data are depicted in Table 3. These complexes exhibited a reversible metal-centered oxidation peak potential in the region of 0.84 ~ 0.46 V. The observed trends between the pairs of Ir(III) complexes

1/**2**, **3**/**4**, and **5**/**6** are consistent with the presence of electron withdrawing and donating substituent on the designated chelate that shifted the potentials to the more positive and less positive directions, i.e. **1** (0.84 V) > **2** (0.78 V), **3** (0.58 V) > **4** (0.46 V), and **5** (0.58 V) > **6** (0.47 V). On the other hand, the trend in oxidation potentials, i.e. **1** (0.84 V) > **2** (0.78 V) > **3** (0.58 V) > **5** (0.58 V), reflected the variation of substituent and main framework of the monoanionic chelates. The trend in oxidation potential is qualitatively in agreement with the calculated HOMO energy level shown in Figures S1 ~ S6 of the supporting information.

Furthermore, upon switching to the cathodic sweep, complexes **1** – **4** showed unambiguous occurrence of irreversible reduction in the narrow region of –2.43 ~ –2.53 V. Apparently, this ligand-centered reduction should take place in the π*-orbital of the 1,3-di(pyridin-2-yl) benzene chelate, L1, L2 and L3. In sharp contrast, the reduction of complexes **5** and **6** can thus be ascribed to the ligand-centered process based at the di-1-isoquinolinyl substituted chelate L4. This is confirmed by shifting the reduction peak potential to less negative region of –2.08 and –2.11 V, and showing reversible electrochemical process, as manifested by their distinctly different, highly conjugated ligating skeleton. Note that the dominant contribution from isoquinolinyl fragments in the lowest lying singlet and triplet states has been pointed out in the computational approach (vide supra).

OLED Device Fabrication. Complexes **1** and **5** were selected as the dopant to investigate electroluminescent (EL) applications because of their higher photoluminescence quantum yields (PLQY). Optimization was achieved by selecting the optimal (i) host material for emission layer (EML), (ii) hole transport layer (HTL), and (iii) electron-transport layer (ETL). In general, hosts with bipolar transport capability allow for the convenient adjustment of carrier recombination as well as carrier balance. In addition, they must possess wide triplet energy gaps (E_T: 2.7 ~ 2.9 eV) which are higher than those of complexes **1** and **5** and thus facilitate adequate

energy transfer as well as exciton confinement. Among three potential hosts being tested, i.e. 3-bis(9-carbazolyl)benzene (mCP), 4,4'-N,N'-dicarbazolebiphenyl (CBP), 2,6-Bis(3-(9H-carbazol-9-yl)phenyl)pyridine (26DCzppy),[42-47] mCP showed the best performances in the present studies. Furthermore, 1,1-bis[(di-4-tolylamino)phenyl]cyclohexane (TAPC) was chosen as the hole-transport layer (HTL),[48, 49] while 3,5,3',5'-tetra(m-pyrid-3-yl)-phenyl[1,1']biphenyl (BP4mPy) and 1,3,5-tri[(3-pyridyl)-phen-3-yl]benzene (TmPyPB) were employed as the ETL because of their great carrier transport abilities and well matched triplet energy gaps.[50-54] Therefore, the OLED architectures consist of ITO/ TAPC (40 nm)/ mCP with 8 wt.% **1** or **5** (30 nm)/ ETL (50 nm)/ LiF (0.8 nm)/ Al (150 nm), where LiF and aluminum serve as the electron injection layer and reflective cathode, respectively. Figure 5 presents the molecular structures of the employed materials along with the energy-level diagram of the OLED devices. Figure 6 and Table 4 summarize the corresponding EL characteristics of OLEDs with employment of BP4mPy (G1 and R1) and TmPyPB (G2 and R2) based ETL.

As showed in Figure 6(a), emission spectral feature of all OLEDs are consistent with the PL of dopants **1** and **5**, indicating that the carrier recombination was well confined within the EML and that exciton diffusion to the adjacent layers had been effectively avoided. However, the EL spectral profiles of both sets of green and red devices underwent a slight variation upon employment of different ETL. We attribute this to the different electron mobility of BP4mPy (~10^{-4} cm^2/Vs) versus that of TmPyPB (~10^{-3} cm^2/Vs),[52, 54] which results in changes of the location of recombination zone and thus the corresponding optical interference.[55] Fortunately, this variation in spectral profiles is considered to be minor and has not affected the emission colors. Accordingly, the green and red devices showed stable CIE coordinates of (0.32, 0.58) and (0.63, 0.37) within a wide range of luminance from 10^2 to 10^4 cd/m^2, respectively.

The current density-voltage-luminance (*J-V-L*) curves revealed higher current

densities for both sets of TmPyPB devices (cf. G2 and R2 in Figure 6(b)) versus the BP4mPy devices (i.e. G1 and R1). Considering both electron transport materials possessing similar LUMO energy levels, the higher current densities should be due to the higher mobility of TmPyPB compared to that of BP4mPy.[52, 54] Consequently, the turn-on voltage of G2 reduced to 3.8 V, which is lower than that of G1 by 0.4 V. In addition, device G2 had a maximum luminance of 15787 cd/m^2 at an operating voltage of 11.0 V, while device G1 only achieved a maximum luminance of 9696 cd/m^2 at 13.8 V. Similarly, the corresponding red-emitting device R2 also showed a lowered turn on voltage versus R1 (3.8 V and 4.4 V), while the TmPyPB device R2 achieved a maximum luminance of 29749 cd/m^2 at 13.0 V, and the BP4mPy device R1 displayed an inferior maximum luminance of 19085 cd/m^2 at 16.0 V, respectively.

Figures 6(c) and (d) showed the trend of efficiencies versus luminescence. As can be seen, the peak efficiencies of BP4mPy device G1 are 12.1%, 37.8 cd/A, and 30.3 lm/W, all of which are lower than those of TmPyPB device G2 (i.e. 13.2 %, 41.4 cd/A, and 35.5 lm/W). On the other hand, in contrast to the green-emitting OLEDs, the BP4mPy device R1 exhibits slightly higher efficiencies (i.e. 15.4 %, 21.0 cd/A, and 16.3 lm/W) than those of the TmPyPB device R2. Device R1 still maintains the forward efficiencies of 14.1 %, 19.1 cd/A, and 8.4 lm/W at 10^2 cd/m^2. The carrier balance achieved in the green and red OLEDs with different ETLs implies that the dopants also influenced the carrier transport in the EML. On the other hand, the EQEs of BP4mPy devices G1 and R1 declined to one-half of their maximal values ($J_{1/2}$) at 17.52 and 48.25 mA/cm^2, for which the corresponding $J_{1/2}$ of TmPyPB devices remained to be 42.74 and 63.43 mA/cm^2.[56-58] The higher $J_{1/2}$ in G2 and R2 is apparently due to the higher mobility of TmPyPB, enabling a longer electron diffusion distance in the EML and thus creating a larger carrier recombination zone compared to the BP4mPy counterpart.[54] Hence, the lower exciton concentration in the EML mitigated the triplet-triplet annihilation. By and large, the high efficiencies obtained in devices G2 and R1 indicated nearly 100% internal quantum efficiency

was achieved in both the green and red devices, which can be attributed to the superior EL properties of phosphors as well as the elaborated architecture design.

Conclusion

In summary, we report the strategic design and synthesis of corresponding neutral, heteroleptic Ir(III) *bis*-tridentate complexes **1** – **6**, for which all of them possess a pair of monoanionic and dianionic chelates, and their emission has been coarse- or fine-tuned from green (490 nm) to red (600 nm) via functionalization. Due to the robust *bis*-tridentate configuration complexes **1** – **6** exhibit intensive phosphorescence with PLQY ranging from 0.22 (**4**) to 0.72 (**1**) in CH_2Cl_2. The representative green and red emissive complexes **1** and **5** have been successfully applied to fabricate OLEDs. A maximum external quantum efficiency of 13.2%, luminance efficiency of 41.4 cd/A, and power efficiency of 35.5 lm/W was obtained for the green OLED (complex **1**), as opposed to 15.4%, 21.0 cd/A, and 16.3 lm/W for the red-emitting device (complex **5**). The high electroluminescence efficiencies suggest great potential of the titled *bis*-tridentate complexes for applications in multicolor displays.

Moreover, owing to the existence of solely the tridentate chelates, this new class of Ir(III) complexes is expected to be chemically more robust compared to the traditional transition-metal phosphors that incorporate chelates with lower denticity. Alternatively, this architecture also affords two orthogonally coordinated chelates, which could result in a more ordered arrangement for the dopants in EML of the multilayered OLEDs, due to their unique conformation. In this way, the out-coupling efficiency is expected to exceed the limit set under the assumption of the randomly deposited dopants, giving significantly improved overall efficiencies. Work on this approach is currently in progress.

Experimental section:

General Information and Materials. All reactions were performed under a nitrogen atmosphere and solvents were distilled from appropriate drying agents prior to use. Commercially available reagents were used without further purification unless otherwise stated. The tridentate monoanionic chelates, i.e. 1,3-difluoro-4,6-di(pyridin-2-yl) benzene (L1-H), 1,3-difluoro-4,6-di(4-*t*-butylpyridin-2-yl) benzene (L2-H), 1,3-di(pyridin-2-yl)-5-*t*-butylbenzene (L3-H), and 1,3-di(isoquinolinyl)-5-*t*-butylbenzene (L4-H), were synthesized from functional 2-bromopyridine (or isoquinoline) and 1,3-benzenediboronic acid bis(pinacol) ester reagents, according to the methods documented in literature,[26, 36] while the dianionic chelates, i.e. 2-(5-trifluoromethyl-1H-pyrazol-3-yl)-6-(4-trifluoromethylphenyl) pyridine (L5-H_2) and 2-(5-trifluoromethyl-1H-pyrazol-3-yl)-6-(4-*t*-butylphenyl) pyridine (L6-H_2) were prepared using the reported functionalization method, followed by hydrazine cyclization.[59 60] ^{1}H and ^{19}F NMR spectra were measured with a Varian Mercury-400 instrument. UV-Vis spectra were recorded on a HITACHI U-3900 spectrophotometer. Detail of measurement of steady-state emission in both solution and solid state was described in our previous reports.[61] Lifetime studies were measured with Edinburgh FL 900 photon-counting system. Electrochemical behaviors were investigated by using cyclic voltammetry (CV) on a CHI621A Electrochemical Analyzer. All measurements were conducted in a 0.1 M $TBAPF_6/CH_2Cl_2$ and THF solution for oxidation and reduction reaction, and reported in volts using FcH/FcH^+ as reference. The Pt electrode and Au(Hg) alloy were selected as the working electrode of oxidation and reduction processes, respectively. The elemental analysis was carried out on a Heraeus CHN-O Rapid Elementary Analyzer. Mass spectra were recorded on a JEOL SX-102A instrument operating in electron impact (EI) or fast atom bombardment (FAB) mode.

Synthesis of dimers $[Ir(Ln)Cl(\mu\text{-}Cl)]_2$, n = 1 – 4.

Ligands L1-H – L4-H and equal molar ratio of $IrCl_3 \cdot 3H_2O$ (5 mmol) were dissolved in a mixed 2-ethoxyethanol (60 mL) and water (20 mL). The mixture was refluxed for 12 h under nitrogen atmosphere. After cooled to RT, the solid that formed was separated by filtration, washed successively with water, ethanol and diethyl ether, and finally dried under vacuum. The products have low solubility in common organic solvents, and were used in subsequent reactions without further purification.

$[Ir(L1)Cl(\mu\text{-}Cl)]_2$, yellow solid, yield: 77%. ^{1}H NMR (400 MHz, d_6-DMSO): δ 9.07 (d, *J* = 5.6 Hz, 4 H), 8.14 (d, *J* = 3.7 Hz, 8 H), 7.65 ~ 7.61 (m, 4 H), 7.25 (t, *J* = 11.6 Hz, 2 H). ^{19}F NMR (376 MHz, d_6-DMSO): δ -106.94 (t, *J* = 12.1 Hz, 4 F).

$[Ir(L2)Cl(\mu\text{-}Cl)]_2$, yellow solid, yield: 75%. ^{1}H NMR of (400 MHz, d_6-DMSO): δ 8.91 (d, *J* = 6.2 Hz, 4 H), 8.03 (s, 4 H), 7.70 (d, *J* = 6.2 Hz, 4 H), 7.24 (t, *J* = 10.5 Hz, 2H), 1.38 (s, 36 H). ^{19}F NMR (376 MHz, d_6-DMSO): δ -107.51 (t, *J* = 11.9 Hz).

$[Ir(L3)Cl(\mu\text{-}Cl)]_2$, orange solid, yield: 81%. ^{1}H NMR (400 MHz, d_6-DMSO): δ 9.01 (d, *J* = 4.8 Hz, 4 H), 8.32 (t, *J* = 7.2 Hz, 4 H), 7.99 (s, 4 H), 7.92 (t, *J* = 7.6 Hz, 4 H), 7.35 (t, *J* = 7.2 Hz, 4 H), 1.44 (s, 18 H).

$[Ir(L4)Cl(\mu\text{-}Cl)]_2$, red solid, yield: 79%. ^{1}H NMR (400 MHz, d_6-DMSO): δ 9.17 (d, *J* = 6.4 Hz, 2 H), 9.09 (t, *J* = 7.6 Hz, 4 H), 8.93 (s, 2 H), 8.56 (d, *J* = 6.4 Hz, 4 H), 8.22 (d, *J* = 8.0 Hz, 4 H), 8.05 (d, *J* = 6.4 Hz, 2 H), 7.96-8.02 (m, 6 H), 7.87-7.94 (m, 4 H), 1.58 (s, 9 H), 1.57 (s, 9 H).

Synthesis of bis-tridentate Ir(III) complexes

A mixture of respective Ir(III) dimers (0.1 mmol), 0.5 equiv. of L5-H_2 or L6-H_2, and 10 equiv. of NaOAc (82 mg, 1 mmol) in decalin (40 ml) was refluxed for 48 h under N_2. The solvent was removed under vacuum and the residue was purified by chromatography (Al_2O_3, hexane/CH_2Cl_2, 1:1) to afford the respective products.

[Ir(L1)(L5)] (**1**), yellow solid, yield: 72%. ^{1}H NMR (400 MHz, $CDCl_3$): δ 8.10 (d, *J* = 4.0 Hz, 2 H), 7.96 (t, *J* = 8.0 Hz, 1 H), 7.81 (d, *J* = 8.0 Hz, 1 H), 7.76 (d, *J* = 8.0 Hz, 1 H), 7.62 ~ 7.55 (m, 4 H), 7.30 (d, *J* = 4.0 Hz, 2 H), 6.99 (d, *J* = 8.0 Hz, 1 H), 6.88 (s, 1 H),

6.73 (t, *J* = 4.0 Hz, 2 H), 6.06 (s, 1 H). ^{19}F NMR (376 MHz, $CDCl_3$): δ -60.15 (s, 3 F), -62.85 (s, 3 F), -107.65 (d, *J* = 12.4 Hz, 2 F). MS [FAB], m/z 816.1, M^+. Anal. Calcd. for $C_{32}H_{16}F_8IrN_5$: C, 47.18; H, 1.98; N, 8.60. Found: C, 46.85; H, 2.18; N, 7.99.

Selected crystal data of **1**: $C_{33}H_{20}F_8IrN_5O$; M = 846.74; monoclinic; space group = $P2_1/n$; *a* = 8.6674(4), *b* = 11.9882(5), *c* = 28.3475(12) Å; β = 98.2998(11)°; *V* = 2914.6(2) Å^3; *Z* = 4; ρ_{calcd} = 1.930 Mg·m^{-3}; *F*(000) = 1640; crystal size = 0.25 x 0.08 x 0.08 mm^3; λ(Mo-K_α) = 0.71073 Å; T = 150(2) K; μ = 4.671 mm^{-1}; 25241 reflections collected, 6691 independent reflections (R_{int} = 0.0619), restraints / parameters = 12 / 454, GOF = 1.181, final $R_1[I > 2\sigma(I)]$ = 0.0601 and wR_2(all data) = 0.1156; Largest diff. peak and hole = 1.504 and -1.497 e·Å^{-3}.

[Ir(L2)(L5)] (**2**), yellow solid, yield: 56%. ^{1}H NMR (400 MHz, $CDCl_3$): δ 8.09 (s, 2 H), 7.93 (d, *J* = 8.0 Hz, 1 H), 7.79 (d, *J* = 8.0 Hz, 1 H), 7.74 (d, *J* = 8.0 Hz, 1 H), 7.61 (d, *J* = 8.0 Hz, 1 H), 7.15 (d, *J* = 8.0 Hz, 2 H), 7.00 (d, *J* = 8.0 Hz, 1 H), 6.89 (s, 1 H), 6.83 (t, *J* = 8.0 Hz, 1 H), 6.72 ~ 6.70 (m, 2 H), 6.12 (s, 1 H), 1.24 (s, 18 H). ^{19}F NMR (376 MHz, $CDCl_3$): δ -59.98 (s, 3 F), -62.68 (s, 3 F), -108.43 (d, *J* = 4.0 Hz, 2 F). MS [FAB], m/z 837.8, M^+. Anal. Calcd. for $C_{40}H_{32}F_8IrN_5$: C, 51.83; H, 3.48; N, 7.56. Found: C, 51.51; H, 3.51; N, 7.63.

[Ir(L3)(L5)] (**3**), yellow solid, yield: 68%. ^{1}H NMR ($CDCl_3$, 400 MHz): δ 8.10 (s, 2 H), 8.01 ~ 7.97 (m, 3 H), 7.90 (d, *J* = 8.0 Hz, 1 H), 7.82 (d, *J* = 8.0 Hz, 1 H), 7.70 (d, *J* = 8.4 Hz, 1 H), 7.63 (t, *J* = 8.4 Hz, 2 H), 7.40 (d, *J* = 5.6 Hz, 2 H), 7.0 (d, *J* = 10.0 Hz, 1 H), 6.91 (s, 1 H),6.77 (t, *J* = 7.2 Hz, 2H) 6.07 (s, 1 H), 1.62 (s, 9 H). ^{19}F NMR ($CDCl_3$, 376 MHz): δ -60.67 (s, 3 F), -63.16 (s, 3 F). MS [FAB], m/z 836.1, $M+H^+$. Anal. Calcd. for $C_{36}H_{26}F_6IrN_5$: C, 51.79; H, 3.14; N, 8.39. Found: C, 52.15; H, 3.41; N, 8.21.

[Ir(L3)(L6)] (**4**), yellow solid, yield: 56%. ^{1}H NMR (400 MHz, $CDCl_3$): δ 7.92 (d, *J* = 7.6 Hz, 2 H), 7.87 (d, *J* = 8.4 Hz, 2 H), 7.78 (d, *J* = 8.0 Hz, 1 H), 7.74 (d, *J* = 7.6 Hz, 1 H), 7.54 (t, *J* = 8.4 Hz, 2 H), 7.44 (d, *J* = 8.4 Hz, 1 H), 7.41 (t, *J* = 7.6 Hz, 1 H), 7.34 (d, *J* = 5.6 Hz, 2 H), 6.95 (s, 1 H), 6.77 (d, *J* = 8.4 Hz, 1 H), 6.70 (t, *J* = 5.6 Hz, 2 H), 5.70 (s, 1 H), 1.24 (s, 9 H), 0.85 (s, 9 H). ^{19}F NMR (376 MHz, $CDCl_3$): δ -59.88 (s, 3 F). MS [FAB], m/z

824, $M+H^+$. Anal. Calcd. for $C_{39}H_{35}F_3IrN_5$: C, 56.92; H, 4.29; N, 8.51. Found: C, 56.76; H, 4.54; N, 8.37.

[Ir(L4)(L5)] (**5**), red solid, yield: 52%. ^{1}H NMR ($CDCl_3$, 400 MHz): δ 9.23 (d, *J* = 8.8 Hz, 2 H), 8.91 (s, 2 H), 8.06 (t, *J* = 8.0 Hz, 1 H) 7.94 (d, *J* = 8.0 Hz, 1 H), 7.90 (d, *J* = 8.0 Hz, 1 H), 7.84 (t, *J* = 8.4 Hz, 2 H), 7.80 (d, *J* = 68 Hz, 2 H), 7.74 (d, *J* = 6.8 Hz, 1 H), 7.73 (t, *J* = 7.6 Hz, 1 H), 7.68 (d, *J* = 8.0 Hz, 1 H), 7.36 (d, *J* = 6.4 Hz, 2 H), 7.15 (d, *J* = 6.4 Hz, 2 H), 6.93 (d, *J* = 7.6 Hz, 2 H), 5.63 (s, 1 H), 1.73 (s, 9 H). ^{19}F NMR ($CDCl_3$, 376 MHz): δ -60.73 (s, 3 F), -63.34 (s, 3 F). MS [FAB], m/z 936, $M+H^+$. Anal. Calcd. for $C_{44}H_{30}F_6IrN_5$: C, 56.52; H, 3.23; N, 7.49. Found: C, 56.23; H, 3.47; N, 7.62.

Selected crystal data of **5**: $C_{45.5}H_{31.5}Cl_{4.5}F_6IrN_5$; M = 1113.98; monoclinic; space group = $P2_1/n$; *a* = 18.5300(3), *b* = 12.8977(2), *c* = 20.1368(4) Å; β = 112.7780(9)°; *V* = 4437.26(13) $Å^3$; *Z* = 4; ρ_{calcd} = 1.668 $Mg\cdot m^{-3}$; *F*(000) = 2188; crystal size = 0.15 × 0.11 × 0.08 mm^3; λ(Mo-K_α) = 0.71073 Å; T = 150(2) K; μ = 3.344 mm^{-1}; 21667 reflections collected, 7806 independent reflections (R_{int} = 0.0554), restraints / parameters = 30 / 567, GOF = 1.069, final $R_1[I > 2\sigma(I)]$ = 0.0446 and wR_2(all data) = 0.1353; Largest diff. peak and hole = 2.130 and -1.050 $e\cdot Å^{-3}$.

[Ir(L4)(L6)] (**6**), red solid, yield: 63%. ^{1}H NMR (400 MHz, $CDCl_3$): δ 9.13 (d, *J* = 8.8 Hz, 2 H), 8.79 (s, 2 H), 7.91 (t, *J* = 7.6 Hz, 1 H), 7.77 ~ 7.73 (m, 4 H), 7.71 (d, *J* = 7.2 Hz, 2 H), 7.64 (t, *J* = 7.6 Hz, 2 H), 7.42 (d, *J* = 8.0 Hz, 1 H), 7.36 (d, *J* = 6.4 Hz, 2 H), 7.04 (d, *J* = 6.4 Hz, 2 H), 6.89 (s, 1 H), 6.68 (d, *J* = 8.0 Hz, 1 H), 5.20 (s, 1 H), 1.68 (s, 9 H), 0.74 (s, 9 H). ^{19}F NMR (376 MHz, $CDCl_3$): δ -60.42 (s, 3 F). MS [FAB], m/z 925, $M+H^+$. Anal. Calcd. for $C_{47}H_{39}F_3IrN_5$: C, 61.16; H, 4.26; N, 7.59. Found: C, 60.92; H, 4.45; N, 7.36.

X-ray Crystallography. All single-crystal X-ray diffraction data were measured on a Bruker Smart CCD diffractometer using λ (Mo Kα) radiation (λ = 0.71073 Å). The data collection was executed using the SMART program. Cell refinement and data reduction were made with the SAINT program. The structure was determined using the SHELXTL/PC program and refined using full matrix least-squares. All

non-hydrogen atoms were refined anisotropically, whereas hydrogen atoms were placed at the calculated positions and included in the final stage of refinements with fixed parameters. CCDC-1042891 and 1042892 contain the supplementary crystallographic data for this paper, which can be obtained from the Cambridge Crystallographic Data Centre via http://www.ccdc.cam.ac.uk.

TD-DFT Calculation

All calculations were performed by Gaussian 09 program.[62] Their ground state structures were first optimized with density functional theory (DFT) at B3LYP/LANL2DZ (Ir) and 6-31G* (H, C, N and F) level. The optimized structures were then used to calculate five lowest singlet and triplet energy optical excitations using the time-dependent density functional theory (TD-DFT) method. A polarizable continuum model (PCM) in Gaussian 09 was applied using dichloromethane as the solvent.

OLED Fabrication. All commercial materials and ITO-coated glass were purchased from Nichem and Lumtec. Glass substrates were cleaned by exposure to an UV-ozone atmosphere for 5 min. The bottom-emitting OLED devices were fabricated using indium tin oxide (ITO) coated glass substrates (< 15 Ω) as the anode, followed by the deposition of multiple organic layers, topped by metal cathode layer. The organic and metal layers were consecutively deposited onto the substrates by thermal evaporation in a vacuum chamber with a base pressure of < 10^{-6} torr without breaking the vacuum. The deposition rate was kept at around 0.1 nm/s. The active area of the device was set to 2 × 2 mm^2, as defined by the shadow mask used for cathode deposition. Current density-voltage-luminance characterization was measured using a Keithley 238 current source-measure unit and a Keithley 6485 picoammeter equipped with a calibrated Si-photodiode. The electroluminescent spectra of the devices were recorded using an Ocean Optics spectrometer.

Acknowledgments. This work was supported by the Ministry of Science and Technology of Taiwan, under the grant NSC-101-2113-M-007-013-MY3. We also thank to the National Center for the High-Performance Computing (NCHC) for the computer time and facilities.

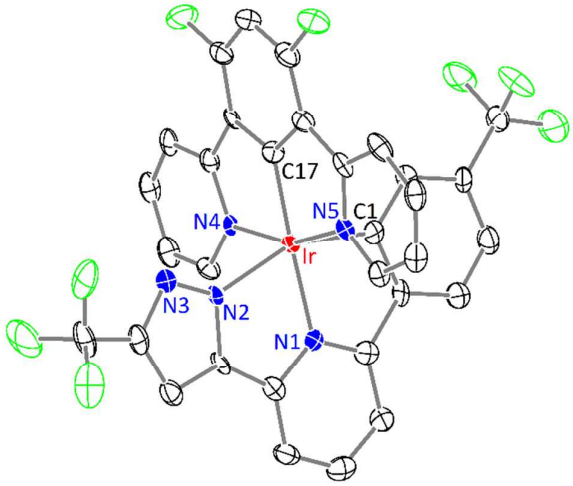

Figure 1. Structural drawing of complex **1** with ellipsoids shown at the 30 % probability, selected bond distances: Ir-C(1) = 2.035(9), Ir-N(1) = 2.063(8), Ir-N(2) = 2.119(6), Ir-N(4) = 2.060(6), Ir-C(17) = 1.919(9) and Ir-N(5) = 2.070(6) Å; selected bond angles: C(1)-Ir-N(2) = 156.7(3), N(4)-Ir-N(5) = 160.5(3) and C(17)-Ir-N(1) = 177.1(3)°.

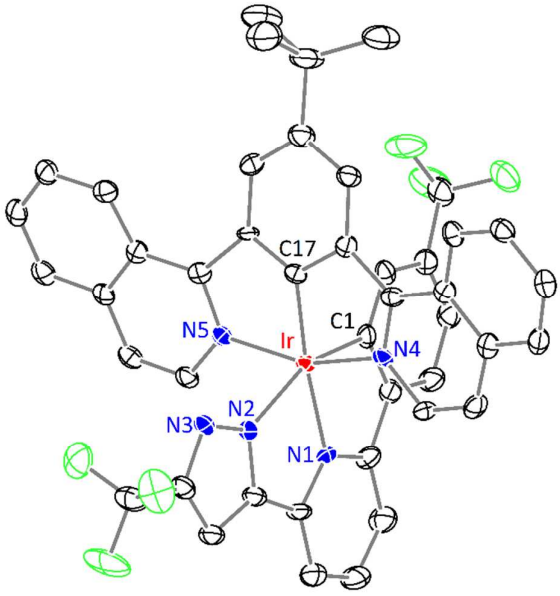

Figure 2. Structural drawing of complex **5** with ellipsoids shown at the 30 % probability, selected bond distances: Ir-C(1) = 2.030(7), Ir-N(1) = 2.072(6), Ir-N(2) = 2.113(6), Ir-N(4) = 2.034(6), Ir-C(17) = 1.926(7) and Ir-N(5) = 2.046(6) Å; selected bond angles: C(1)-Ir-N(2) = 156.0(3), N(4)-Ir-N(5) = 159.1(2) and C(17)-Ir-N(1) =

172.6(3)°.

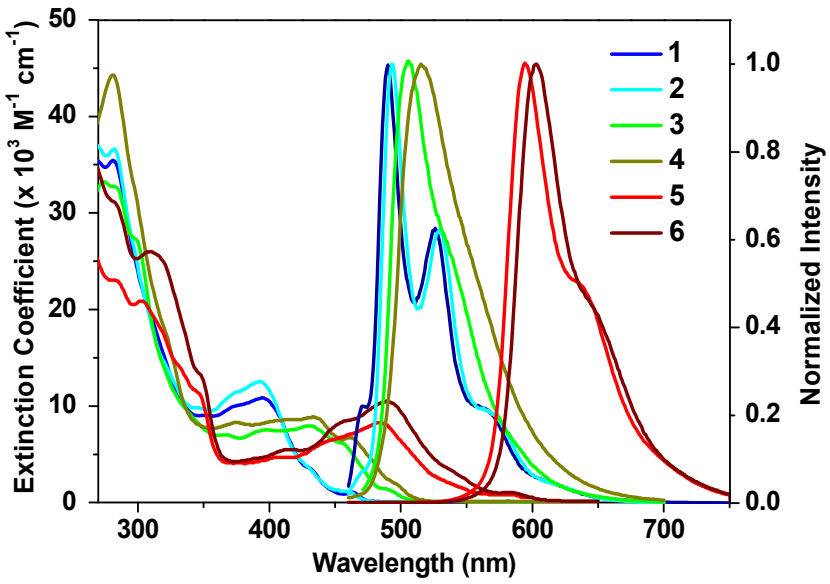

Figure 3. Absorption and normalized emission spectra of complex **1** – **6** recorded in CH_2Cl_2 solution at RT.

	HOMO	LUMO	LUMO+1
1	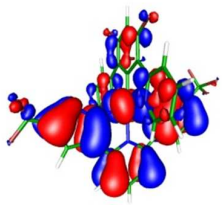	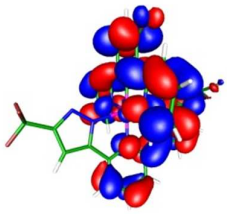	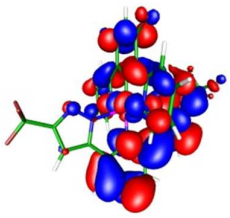
2	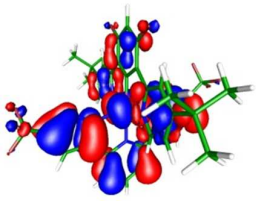	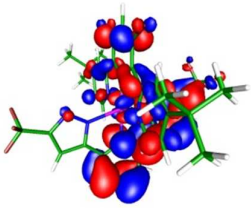	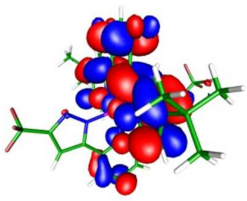
3	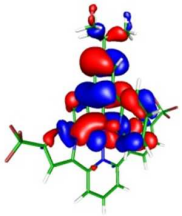	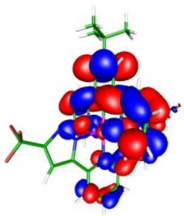	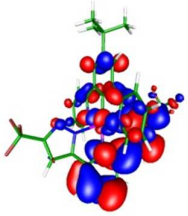
4	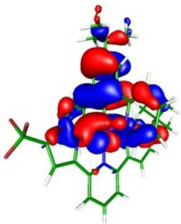	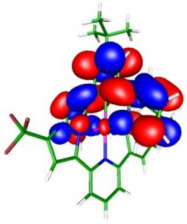	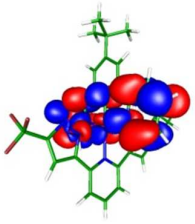
5	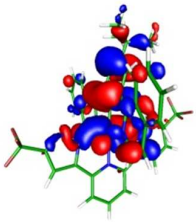	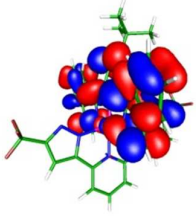	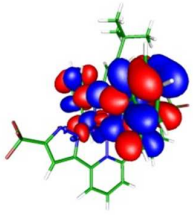
6	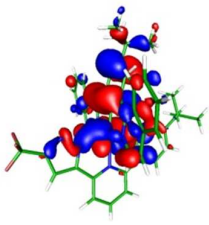	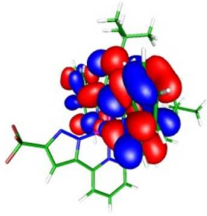	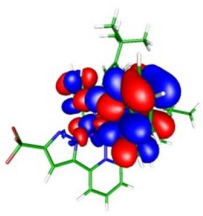

Figure 4. Frontier molecular orbitals (HOMO, LUMO and LUMO+1) in the lowest optical transitions for complexes **1** – **6**.

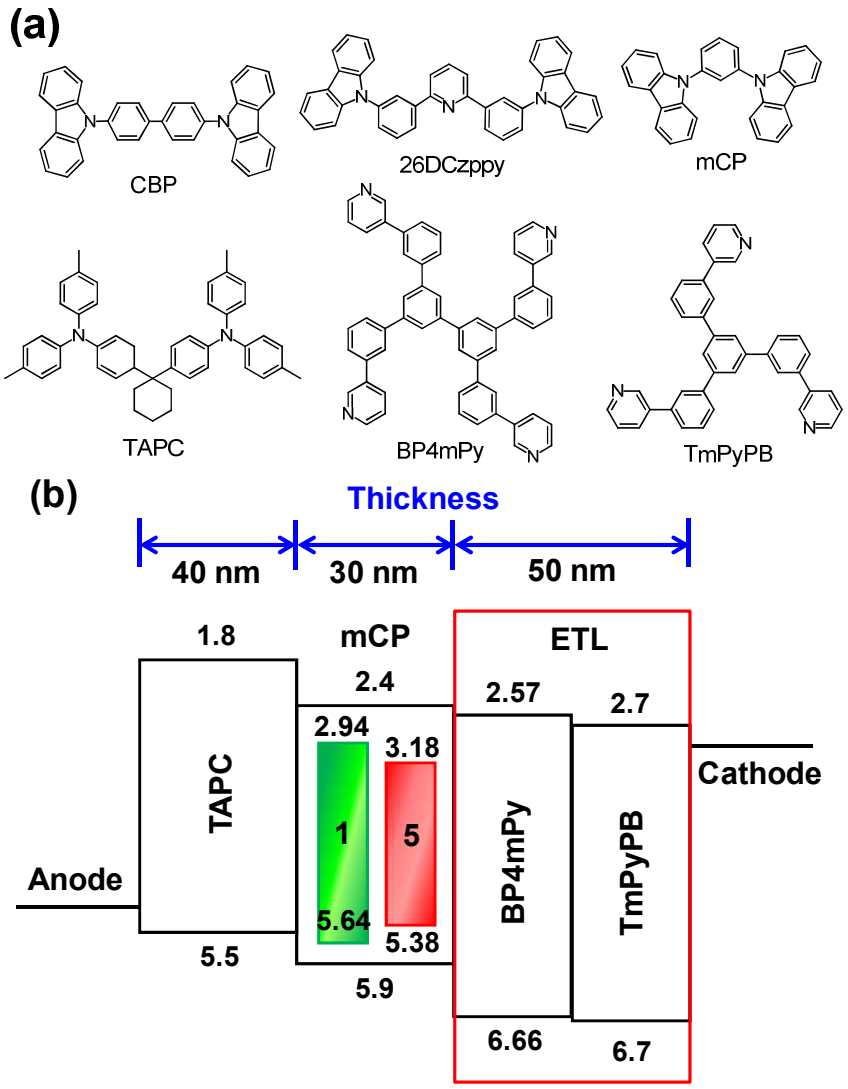

Figure 5. (a) Material chemical structures; (b) energy level diagram of tested green and red OLEDs with different electron transport layers.

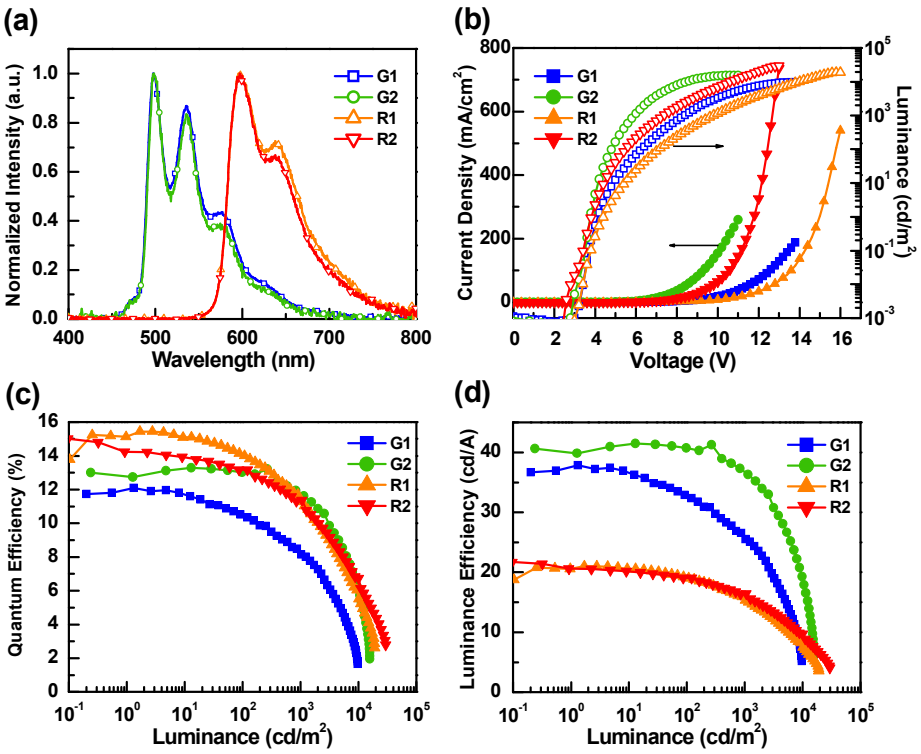

Figure 6. (a) EL spectra of green and red OLEDs; (b) current density-voltage-luminance (*J*-*V*-*L*) curves; (c) external quantum efficiency vs. luminance; (d) luminance efficiency vs. luminance for devices G1, G2, R1, and R2.

Table 1. Photophysical data of complex **1 – 6** recorded in CH_2Cl_2 at RT.

	abs λ/nm [a] ($\varepsilon \times 10^{-4}$ $M^{-1}\cdot cm^{-1}$)	em λ_{max} (nm) [a]	τ_{obs} (μs)[a]	em Φ (%)	k_r [d] ($\times 10^5$ s^{-1})	k_{nr} [d] ($\times 10^5$ s^{-1})
1	281 (3.54), 373 (1.00), 395 (1.08), 464 (0.11)	490, 526, 570 (sh)	1.81	72[b]	3.98	1.54
2	282 (3.66), 374 (1.14), 392 (1.25), 460 (0.12)	493, 529, 571 (sh)	3.37	64[b]	1.90	1.07
3	284 (3.26), 397 (0.75), 430 (0.80), 456 (0.61)	505, 540 (sh)	1.27	25[b]	1.97	5.90
4	281 (4.43), 374 (0.83), 436 (0.88), 463 (0.67)	515, 556 (sh)	0.81	22[b]	2.72	9.63
5	304 (2.09), 347 (1.12), 486 (0.83), 580 (0.08)	594, 641 (sh)	1.77	63[c]	3.56	2.09
6	310 (2.60), 457 (0.85), 490 (1.05), 580 (0.11)	602, 650 (sh)	1.73	43[c]	2.49	3.29

[a] UV-Vis spectra, photoluminescence spectra, lifetime and quantum yields were recorded in CH_2Cl_2 at a conc. of 10^{-5} M. [b] Coumarin (C102) in EtOH as the reference standard (0.764). [c] 4-(Dicyanomethylene)-2-methyl-6-(4-dimethylaminostyryl)-4*H*-pyran in EtOH as the reference standard (0.435). [d] $(k_r + k_{nr}) = 1 / \tau_{obs}$ where τ_{obs} is the emission lifetime. The radiative decay rate constant k_r is calculated by Φ (%) = $k_r / (k_r + k_{nr})$.

Table 2. The calculated energy levels and orbital transition analyses of complexes **1** – **6**. We only list the optical transition involving the largest contribution percentage.

	State	λ (nm)	f	Assignments	MLCT
1	T_1	454.6	0	HOMO → LUMO+1 (39%)	20.16%
	S_1	389.8	0.0338	HOMO → LUMO (47%)	28.56%
2	T_1	456.1	0	HOMO → LUMO (56%)	21.81%
	S_1	392.3	0.0296	HOMO → LUMO (84%)	30.52%
3	T_1	483.7	0	HOMO → LUMO (83%)	29.21%
	S_1	415.9	0.1214	HOMO → LUMO (94%)	29.74%
4	T_1	490.8	0	HOMO → LUMO (94%)	30.63%
	S_1	421.8	0.1303	HOMO → LUMO (91%)	31.38%
5	T_1	567.3	0	HOMO → LUMO (30%)	22.65%
	S_1	473.8	0.2674	HOMO → LUMO (96%)	26.35%
6	T_1	574.8	0	HOMO → LUMO (44%)	20.90%
	S_1	482.5	0.2437	HOMO → LUMO (91%)	26.04%

Table 3. Electrochemical data of complex **1** – **6** recorded in CH_2Cl_2 at RT.

sample	E_{pa}^{ox} (V)[a] [ΔE_P]	$E_{1/2}^{re}$ (V)[a] [ΔE_P]	HOMO (eV)[b]	E_{00} (eV)	LUMO (eV)[b]
1	0.84 [0.09]	–2.43 [irr][c]	5.64	2.70	2.94
2	0.78 [0.08]	–2.45 [irr]	5.58	2.70	2.88
3	0.58 [0.12]	–2.43 [irr]	5.38	2.60	2.78
4	0.46 [0.08]	–2.53 [irr]	5.26	2.57	2.69
5	0.58 [0.08]	–2.08 [0.14]	5.38	2.20	3.18
6	0.47 [0.10]	–2.11 [0.13]	5.27	2.23	3.04

[a] $E_{1/2}$ (mV) refers to $[(E_{pa}+E_{pc})/2]$ where E_{pa} and E_{pc} are the anodic and cathodic peak potentials referenced to the FcH^+/FcH couple; ΔE_p is defined as E_{ap} (anodic peak potential) – E_{cp} (cathodic peak potential) and these data are quoted in mV. [b] HOMO = $|-4.8 - E_{1/2}^{ox}|$. LUMO = HOMO – E_{00}. E_{00} = onset of emission. [c] irr denotes irreversible process.

Table 4. EL characteristics of tested devices with different emitters.

device		**G1**	**G2**	**R1**	**R2**
dopant		**1**		**5**	
ETL		**BP4mPy**	**TmPyPB**	**BP4mPy**	**TmPyPB**
external quantum efficiency (%)	[a]	12.1	13.2	15.4	15.0
	[b]	10.5	13.0	14.1	13.2
luminescence efficiency (cd/A)	[a]	37.8	41.4	21.0	21.7
	[b]	32.9	40.7	19.1	19.1
power efficiency (lm/W)	[a]	30.3	35.5	16.3	20.1
	[b]	16.7	26.6	8.4	10.9
V_{on} (V)	[c]	4.2	3.8	4.4	3.8
max. luminance (cd/m^2) [voltage]		9696 [13.8 V]	15787 [11.0 V]	19085 [16.0 V]	29749 [13.0 V]
CIE1931 coordinates	[b]	(0.315, 0.576)	(0.305, 0.582)	(0.632, 0.365)	(0.631, 0.366)
	[d]	(0.315, 0.576)	(0.305, 0.580)	(0.631, 0.367)	(0.629, 0.369)
	[e]	–	(0.303, 0.582)	(0.628, 0.369)	(0.628, 0.371)

[a] Maximum efficiency; [b] recorded at 10^2 cd/m^2; [c] turn-on voltage measured at 1 cd/m^2; [d] measured at 10^3 cd/m^2; [e] measured at 10^4 cd/m^2.

1. M. A. Baldo, D. F. O'Brien, Y. You, A. Shoustikov, S. Sibley, M. E. Thompson and S. R. Forrest, *Nature*, 1998, **395**, 151.
2. Y. You and S. Y. Park, *Dalton Trans.*, 2009, 1267.
3. Y. Chi and P.-T. Chou, *Chem. Soc. Rev.*, 2010, **39**, 638.
4. G. Zhou, W.-Y. Wong and X. Yang, *Chem. Asian J.*, 2011, **6**, 1706.
5. A. Tsuboyama, H. Iwawaki, M. Furugori, T. Mukaide, J. Kamatani, S. Igawa, T. Moriyama, S. Miura, T. Takiguchi, S. Okada, M. Hoshino and K. Ueno, *J. Am. Chem. Soc.*, 2003, **125**, 12971.
6. A. R. G. Smith, J. L. Ruggles, H. Cavaye, P. E. Shaw, T. A. Darwish, M. James, I. R. Gentle and P. L. Burn, *Adv. Funct. Mater.*, 2011, **21**, 2225.
7. A. Graf, P. Liehm, C. Murawski, S. Hofmann, K. Leo and M. C. Gather, *J. Mater. Chem. C*, 2014.
8. A. F. Rausch, M. E. Thompson and H. Yersin, *J. Phys. Chem. A*, 2009, **113**, 5927.
9. E. D. Baranoff and B. Curchod, *Dalton Trans.*, 2015, DOI: 10.1039/C1034DT02991G.
10. Y. Chi and P.-T. Chou, *Chem. Soc. Rev.*, 2007, **36**, 1421.
11. P.-T. Chou and Y. Chi, *Chem. Eur. J.*, 2007, **13**, 380.
12. Y. Chi, B. Tong and P.-T. Chou, *Coord. Chem. Rev.*, 2014, **281**, 1.

13. A. J. Wilkinson, H. Puschmann, J. A. K. Howard, C. E. Foster and J. A. G. Williams, *Inorg. Chem.*, 2006, **45**, 8685.
14. T. Yutaka, S. Obara, S. Ogawa, K. Nozaki, N. Ikeda, T. Ohno, Y. Ishii, K. Sakai and M.-a. Haga, *Inorg. Chem.*, 2005, **44**, 4737.
15. S. Obara, M. Itabashi, F. Okuda, S. Tamaki, Y. Tanabe, Y. Ishii, K. Nozaki and M.-a. Haga, *Inorg. Chem.*, 2006, **45**, 8907.
16. L. Yang, F. Okuda, K. Kobayashi, K. Nozaki, Y. Tanabe, Y. Ishii and M.-a. Haga, *Inorg. Chem.*, 2008, **47**, 7154.
17. M. Ashizawa, L. Yang, K. Kobayashi, H. Sato, A. Yamagishi, F. Okuda, T. Harada, R. Kuroda and M. Haga, *Dalton Trans.*, 2009, 1700.
18. J. Kuwabara, T. Namekawa, M.-a. Haga and T. Kanbara, *Dalton Trans.*, 2012, **41**, 44.
19. J. A. G. Williams, A. J. Wilkinson and V. L. Whittle, *Dalton Trans.*, 2008, 2081-2099.
20. Y. Koga, M. Kamo, Y. Yamada, T. Matsumoto and K. Matsubara, *Eur. J. Inorg. Chem.*, 2011, 2869.
21. J.-L. Chen, Y.-H. Wu, L.-H. He, H.-R. Wen, J. Liao and R. Hong, *Organometallics*, 2010, **29**, 2882.
22. V. L. Whittle and J. A. G. Williams, *Dalton Trans.*, 2009, 3929.
23. W.-W. Yang, Y.-W. Zhong, S. Yoshikawa, J.-Y. Shao, S. Masaoka, K. Sakai, J. Yao and M.-a. Haga, *Inorg. Chem.*, 2011, **51**, 890.
24. N. Darmawan, C.-H. Yang, M. Mauro, M. Raynal, S. Heun, J. Pan, H. Buchholz, P. Braunstein and L. De Cola, *Inorg. Chem.*, 2013, **52**, 10756.
25. L. F. Gildea, A. S. Batsanov and J. A. G. Williams, *Dalton Trans.*, 2013, **42**, 10388.
26. P. Brulatti, R. J. Gildea, J. A. K. Howard, V. Fattori, M. Cocchi and J. A. G. Williams, *Inorg. Chem.*, 2012, **51**, 3813.
27. A. J. Wilkinson, A. E. Goeta, C. E. Foster and J. A. G. Williams, *Inorg. Chem.*, 2004, **43**, 6513.
28. K.-L. Wu, C.-H. Li, Y. Chi, J. N. Clifford, L. Cabau, E. Palomares, Y.-M. Cheng, H.-A. Pan and P.-T. Chou, *J. Am. Chem. Soc.*, 2012, **134**, 7488.
29. C.-C. Chou, P.-H. Chen, F.-C. Hu, Y. Chi, S.-T. Ho, J.-J. Kai, S.-H. Liu and P.-T. Chou, *J. Mater. Chem. A*, 2014, **2**, 5418.
30. J.-L. Liao, Y. Chi, Y.-D. Su, H.-X. Huang, C.-H. Chang, S.-H. Liu, G.-H. Lee and P.-T. Chou, *J. Mater. Chem. C*, 2014, **2**, 6269.
31. J. A. G. Williams, *Chem. Soc. Rev.*, 2009, **38**, 1783.
32. J.-Y. Hung, C.-H. Lin, Y. Chi, M.-W. Chung, Y.-J. Chen, G.-H. Lee, P.-T. Chou, C.-C. Chen and C.-C. Wu, *J. Mater. Chem.*, 2010, **20**, 7682.
33. C.-H. Lin, Y.-Y. Chang, J.-Y. Hung, C.-Y. Lin, Y. Chi, M.-W. Chung, C.-L. Lin, P.-T. Chou, G.-H. Lee, C.-H. Chang and W.-C. Lin, *Angew. Chem. Int. Ed.*, 2011, **50**, 3182.
34. C.-H. Lin, Y.-C. Chiu, Y. Chi, Y.-T. Tao, L.-S. Liao, M.-R. Tseng and G.-H. Lee, *Organometallics*, 2012, **31**, 4349.
35. S.-W. Wang, C.-C. Chou, F.-C. Hu, K.-L. Wu, Y. Chi, J. N. Clifford, E. J. Palomares,

S.-H. Liu, P.-T. Chou, T. C. Wei and T. Y. Hsiao, *J. Mater. Chem. A*, 2014, **2**, 17618.
36. Z. Wang, E. Turner, V. Mahoney, S. Madakuni, T. Groy and J. Li, *Inorg. Chem.*, 2010, **49**, 11276.
37. T.-C. Lee, J.-Y. Hung, Y. Chi, Y.-M. Cheng, G.-H. Lee, P.-T. Chou, C.-C. Chen, C.-H. Chang and C.-C. Wu, *Adv. Funct. Mater.*, 2009, **19**, 2639.
38. J. Brooks, Y. Babayan, S. Lamansky, P. I. Djurovich, I. Tsyba, R. Bau and M. E. Thompson, *Inorg. Chem.*, 2002, **41**, 3055.
39. F.-M. Hwang, H.-Y. Chen, P.-S. Chen, C.-S. Liu, Y. Chi, C.-F. Shu, F.-I. Wu, P.-T. Chou, S.-M. Peng and G.-H. Lee, *Inorg. Chem.*, 2005, **44**, 1344.
40. C.-H. Lin, Y. Chi, M.-W. Chung, Y.-J. Chen, K.-W. Wang, G.-H. Lee, P.-T. Chou, W.-Y. Hung and H.-C. Chiu, *Dalton Trans.*, 2011, **40**, 1132.
41. S. C. F. Kui, F.-F. Hung, S.-L. Lai, M.-Y. Yuen, C.-C. Kwok, K.-H. Low, S. S.-Y. Chui and C.-M. Che, *Chem. Eur. J.*, 2012, **18**, 96.
42. B. E. Koene, D. E. Loy and M. E. Thompson, *Chem. Mater.*, 1998, **10**, 2235.
43. D. F. O'Brien, M. A. Baldo, M. E. Thompson and S. R. Forrest, *Appl. Phys. Lett.*, 1999, **74**, 442.
44. R. J. Holmes, S. R. Forrest, Y.-J. Tung, R. C. Kwong, J. J. Brown, S. Garon and M. E. Thompson, *Appl. Phys. Lett.*, 2003, **82**, 2422.
45. T. Tsuboi, S.-W. Liu, M.-F. Wu and C.-T. Chen, *Org. Electron.*, 2009, **10**, 1372.
46. S.-J. Su, H. Sasabe, T. Takeda and J. Kido, *Chem. Mater.*, 2008, **20**, 1691.
47. C. Cai, S.-J. Su, T. Chiba, H. Sasabe, Y.-J. Pu, K. Nakayama and J. Kido, *Org. Electron.*, 2011, **12**, 843.
48. K. Goushi, R. Kwong, J. J. Brown, H. Sasabe and C. Adachi, *J. Appl. Phys.*, 2004, **95**, 7798.
49. Y. Zheng, S.-H. Eom, N. Chopra, J. Lee, F. So and J. Xue, *Appl. Phys. Lett.*, 2008, **92**, 223301.
50. S.-J. Su, D. Tanaka, Y.-J. Li, H. Sasabe, T. Takeda and J. Kido, *Org. Lett.*, 2008, **10**, 941.
51. S.-J. Su, T. Chiba, T. Takeda and J. Kido, *Adv. Mater.*, 2008, **20**, 2125.
52. S.-J. Su, Y. Takahashi, T. Chiba, T. Takeda and J. Kido, *Adv. Funct. Mater.*, 2009, **19**, 1260.
53. A. Endo, K. Sato, K. Yoshimura, T. Kai, A. Kawada, H. Miyazaki and C. Adachi, *Appl. Phys. Lett.*, 2011, **98**, 083302.
54. C.-H. Chang, C.-L. Ho, Y.-S. Chang, I.-C. Lien, C.-H. Lin, Y.-W. Yang, J.-L. Liao and Y. Chi, *J. Mater. Chem. C*, 2013, **1**, 2639.
55. C.-L. Lin, H.-W. Lin and C.-C. Wu, *Appl. Phys. Lett.*, 2005, **87**, 021101.
56. S.-J. Su, E. Gonmori, H. Sasabe and J. Kido, *Adv. Mater.*, 2008, **20**, 4189.
57. H. Sasabe, J.-i. Takamatsu, T. Motoyama, S. Watanabe, G. Wagenblast, N. Langer, O. Molt, E. Fuchs, C. Lennartz and J. Kido, *Adv. Mater.*, 2010, **22**, 5003.
58. D. Curiel, M. Mas-Montoya, C.-H. Chang, P.-Y. Chen, C.-W. Tai and A. Tarraga, *J. Mater. Chem. C*, 2013, **1**, 3421.
59. C.-W. Hsu, S.-T. Ho, K.-L. Wu, Y. Chi, S.-H. Liu and P.-T. Chou, *Energy Environ. Sci.*, 2012, **5**, 7549.

60. Y. Chi, K.-L. Wu and T.-C. Wei, *Chem. Asian J.*, 2015, DOI: 10.1002/asia.201403261.
61. P.-T. Chou, W.-S. Yu, Y.-M. Cheng, S.-C. Pu, Y.-C. Yu, Y.-C. Lin, C.-H. Huang and C.-T. Chen, *J. Phys. Chem. A*, 2004, **108**, 6487.
62. M. J. Frisch, G. W. Trucks, H. B. Schlegel, G. E. Scuseria, M. A. Robb, J. R. Cheeseman, G. Scalmani, V. Barone, B. Mennucci, G. A. Petersson, H. Nakatsuji, M. Caricato, X. Li, H. P. Hratchian, A. F. Izmaylov, J. Bloino, G. Zheng, J. L. Sonnenberg, M. Hada, M. Ehara, K. Toyota, R. Fukuda, J. Hasegawa, M. Ishida, T. Nakajima, Y. Honda, O. Kitao, H. Nakai, T. Vreven, J. A. Montgomery, J. E. Peralta, F. Ogliaro, M. Bearpark, J. J. Heyd, E. Brothers, K. N. Kudin, V. N. Staroverov, R. Kobayashi, J. Normand, K. Raghavachari, A. Rendell, J. C. Burant, S. S. Iyengar, J. Tomasi, M. Cossi, N. Rega, J. M. Millam, M. Klene, J. E. Knox, J. B. Cross, V. Bakken, C. Adamo, J. Jaramillo, R. Gomperts, R. E. Stratmann, O. Yazyev, A. J. Austin, R. Cammi, C. Pomelli, J. W. Ochterski, R. L. Martin, K. Morokuma, V. G. Zakrzewski, G. A. Voth, P. Salvador, J. J. Dannenberg, S. Dapprich, A. D. Daniels, Farkas, J. B. Foresman, J. V. Ortiz, J. Cioslowski and D. J. Fox, *Gaussian 09, Revision A.1; Gaussian Inc.*, 2009, Wallingford, CT.

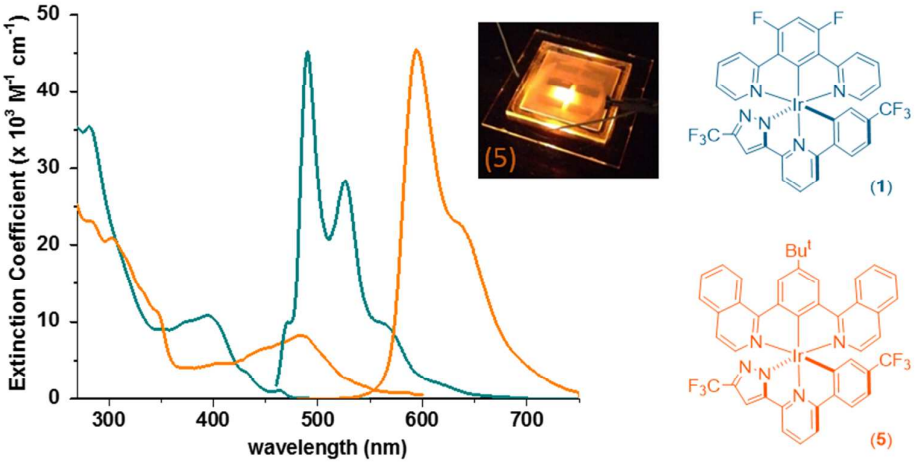

Emissive Ir(III) complexes bearing two tridentate chelates were synthesized. The multiple coordination mode of chelate warrants a new class of metal based phosphors for OLED applications.